Monolithic high contrast grating on GaSb/AlAsSb based epitaxial structures for mid-infrared wavelength applications

A. SCHADE,[1] A. BADER,[1] T. HUBER,[1] S. KUHN,[1] T. CZYSZANOWSKI,[2] A. PFENNING,[1,3] M. RYGAŁA,[4] T. SMOŁKA,[4] M. MOTYKA,[4] G. SĘK,[4] F. HARTMANN,[1,*] AND S. HÖFLING[1]

[1]*Technische Physik, Physikalisches Institut and Wilhelm-Conrad-Röntgen Research Center for Complex Material Systems, Universität Würzburg, Am Hubland, D-97074 Würzburg, Germany*
[2]*Technical University of Lodz, Laboratory of Photonics Institute of Physics, 90-924 Lodz, Poland*
[3]*Stewart Blusson Quantum Matter Institute, University of British Columbia, Vancouver, British Columbia V6T 1Z4, Canada*
[4]*Laboratory for Optical Spectroscopy of Nanostructures, Department of Experimental Physics, Faculty of Fundamental Problems of Technology, Wrocław University of Science and Technology, Wybrzeże Wyspiańskiego 27, 50-370 Wrocław, Poland*
[*]*Fabian.Hartmann@physik.uni-wuerzburg.de*

Abstract: We demonstrate monolithic high contrast gratings (MHCG) based on GaSb/AlAs$_{0.08}$Sb$_{0.92}$ epitaxial structures with sub-wavelength gratings enabling high reflection of unpolarized mid-infrared radiation at the wavelength range from 2.5 to 5 µm. We study the reflectivity wavelength dependence of MHCGs with ridge widths ranging from 220 to 984 nm and fixed 2.6 µm grating period and demonstrate that peak reflectivity of above 0.7 can be shifted from 3.0 to 4.3 µm for ridge widths from 220 to 984 nm, respectively. Maximum reflectivity of up to 0.9 at 4 µm can be achieved. The experiments are in good agreement with numerical simulations, confirming high process flexibility in terms of peak reflectivity and wavelength selection. MHCGs have hitherto been regarded as mirrors enabling high reflection of selected light polarization. With this work, we show that thoughtfully designed MHCG yields high reflectivity for both orthogonal polarizations simultaneously. Our experiment demonstrates that MHCGs are promising candidates to replace conventional mirrors like distributed Bragg reflectors to realize resonator based optical and optoelectronic devices such as resonant cavity enhanced light emitting diodes and resonant cavity enhanced photodetectors in the mid-infrared spectral region, for which epitaxial growth of distributed Bragg reflectors is challenging.

1. Introduction

Optoelectronic devices operating in the mid-infrared (MIR) wavelength region are of special interest in many technological fields such as thermal imaging and gas sensing applications like tunable laser absorption spectroscopy [1,2]. The wavelength range between 2 and 7 µm is particularly interesting as it hosts strong absorption lines of different environmentally and industrially relevant gases like hydrocarbons, carbon oxides and nitrous oxides. Here, light detecting and light emitting devices such as interband cascade infrared photodetectors (ICIP) [3,4] or interband cascade lasers (ICL) [5,6,7] are of great interest as they show superior figures of merit compared to alternative architectures. ICIPs show reduced noise behavior compared to single-stage photodetectors and ICLs offer usually significantly lower threshold current and

power consumption in the MIR, compared to type-I diode laser diodes or quantum cascade lasers (QCL). Since not every application has the need of monochromatic light emission, for example when using narrow band detectors [8] or hollow core fibers [9], light emitting diodes (LEDs) can be incoherent, broadband emitting alternatives, which convince in cost optimization. The interband cascade technology used in LEDs (ICLEDs) [10–12] can cover these applications for wavelengths analogous to ICLs.

By combining resonant optical cavities with conventional LED technology, the spontaneous emission based optical output can be spatially redirected and its intensity highly increased. The resulting RCLEDs were first experimentally realized in 1990 in a semiconductor system based on GaAs at emission wavelengths around 830 nm [13], followed by demonstrations in several different material systems in single and multimode resonant cavities covering the visible, near infrared and mid-infrared wavelength region [14–18]. On the other hand, resonant cavity enhanced (RCE) photodetectors show highly increased amplitude of the resonant field within the cavity and narrowband detection [19,20].

Conventional optical resonators with sufficiently high reflectivity in the mid-infrared rely on top and bottom distributed Bragg reflectors (DBR) [21] that are either purely epitaxially grown [22,23], dielectric or combination of both [24,25]. In this context, the quality of epitaxially grown mirrors is one limiting factor in its realization. Since the reflectivity of doped AlAsSb/GaSb DBRs is limited by free-carrier absorption [26], replacing the doped top DBR is necessary to achieve high external efficiency [26]. This is also important in cost driven aspects as it allows to considerably reduce the growth time (since DBR thicknesses in the MIR are very large) and increase production volume. Dielectric mirrors such as ZnS/Ge [26] or Ge/Al$_2$O$_3$ [24] or metal-based mirrors [27,12] can replace conventional epitaxially grown top DBRs and provide high reflectivities with the use of just a few mirror pairs [24,26,28] but they lack in additional process steps and with use of additional, different material systems. Mateus et al. [29] showed that a high index contrast grating (HCG) etched in thin epitaxial layer can show high reflectivities over broad wavelength regions [30]. In 2007 the first VCSEL employing HCG structures was demonstrated using the index contrast between Al$_{0.6}$Ga$_{0.4}$As and air [31,32]. HCGs offer high reflectivities over broad wavelength regions compared to the narrow stopband obtained with conventional DBRs and provide additional flexibility due to the post growth manufacturing routine and polarization selection. In 2015 monolithic high-index contrast gratings (MHCG) were proposed for GaAs using gratings etched monolithically in the surface of epitaxial grown layers with 100% reflectivity theoretically demonstrated in [33] and 95% reflectivity demonstrated experimentally in [34].

In this paper we extend the limits of high contrast grating mirrors usability by demonstration of unpolarized light high reflectivity by MHCG. Our design is based on GaSb/AlAs$_{0.08}$Sb$_{0.92}$ epitaxial structures with ridge widths from 220 to 984 nm and 2.6 µm grating period showing enhanced unpolarized light reflectivity in the wavelength range from 2.5 to 5 µm with maximum values of up to 0.9. This presents a first step towards antimony-based high contrast gratings for replacing conventional mirrors for RCLED structures such as ICLEDs and other optoelectronic devices in the MIR spectral range. Polarization dependent transmission measurements via Fourier-transform infrared spectroscopy through the backside of the samples show good agreement with numerical simulations. The design shows flexibility in terms of wavelength selection with a single exposure and etching step and post growth reflectivity adaption.

2. Sample fabrication and processing

The sample was grown via molecular beam epitaxy (MBE) in an Eiko EV 100S machine. The MBE main chamber is equipped with valved group-V cracker effusion cells for antimony (Sb) and arsenic (As) and conventional effusion cells for group-III elements such as gallium (Ga) and aluminum (Al). The structure was grown on a tellurium n-doped GaSb (001) single side

polished wafer. After two minutes of oxide desorption at 580 °C under Sb pressure a 150 nm thick GaSb buffer was grown to smoothen the surface. A 452 nm thick lattice-matched low- index $AlAs_{0.08}Sb_{0.92}$ (n_{AlAsSb} = 3.13) layer was grown on top, followed by 764 nm high-index GaSb (n_{GaSb} = 3.78). Both layers were grown at a substrate temperature of 485°C. After the epitaxial growth, the sample was cleaned and processed. Figure 1(a) shows a schematic of the epitaxial and processed sample layout with the grating period L and ridge width w. Electron beam lithography and dry chemical etching were used to define 537 ± 5 nm nm deep gratings with different ridge widths of w = 220, 488, 785 and 984 ± 5 nm and a fixed grating period of L = 2.6 μm within an area of 4 × 4 mm. The sample was designed to achieve maximum reflectivity of unpolarized light in the MIR wavelength range between 2.5 and 5 μm [29,30].

3. Experimental and simulated data

The samples were designed to realize peak reflectivities in the sweet spot operation wavelength range of ICLs within 2.5-5 μm [7]. In the numerical calculations, we simulate a single period of the structure demonstrated in Fig. 1(a) with a grating stripe of infinite length and periodic boundary conditions that elongate the periodicity of the grating to infinity. We also assume semi-infinite thickness of air above the MHCG and a semi-infinite GaSb layer beneath the structure. To determine the optical power transmittance and reflectance of the gratings, we use the plane-wave reflection transformation method (PWRTM) [35]. We consider two orthogonal polarizations: transverse-electric (TE), for which electric field of electromagnetic wave is parallel to the stripes, and transverse magnetic (TM), where the magnetic component of the electromagnetic field is parallel to the grating stripes. We calculate the transmittivity and reflectivity of unpolarized light as the mean value of intensities for both TE and TM polarizations since Maxwell's equations are linear and the general solution is a superposition of both orthogonal polarizations [36]. The method's accuracy has been validated in numerous analyses [37,38] by comparison with experimental reflection spectra of MHCGs. In the simulation and for all experiments, the reflectivity was determined by illuminating the structure under normal incidence from the substrate side. Figure 1(c) shows a colourmap of the numerically calculated reflection of unpolarized light for gratings with four different ridge widths w in the wavelength range from 2.5–5.0 μm for different etchings depths over wavelength. Absorption was neglected in the simulation. With increasing ridge width from 220 to 984 nm the maximal reflection is shifted from 2.9 μm to 4.0 μm, showing the high flexibility of wavelength selection with post growth processing. Theoretical reflection values of up to 0.89 can be achieved with the 785 nm grating width at 3.8 μm. To achieve comparable values with conventional $GaSb/AlAs_{0.08}Sb_{0.92}$ DBRs, up to 15 mirror pairs are necessary due to the low index contrast between GaSb and $AlAs_{0.08}Sb_{0.92}$. With period thickness of around 500 nm for each pair, this results in increased growth time and related increased costs. With the possibility of post growth MHCG implementation, with variable parameters enabling modification of resonant wavelength and polarization selectivity, the yield of functional wafers can increase significantly since conventional DBRs do not offer this possibility.

The unpolarized (polarized) measurements, were performed at two different measuring setups (see [39,40,41] for more technical details and description of the advantages of this approach). A Bruker IFS 66 v/s (Vertex 80 v) FTIR spectrometer equipped with a liquid nitrogen cooled MCT detector was used to measure transmission spectra of the MHCG and the reference samples with a resolution of 4 cm^{-1}. The transmission was measured under normal (12° to normal) incidence on the backside of the samples and at atmospheric pressure (at decreased pressure (approx. 3 hPa) to minimize atmospheric gasses absorption) and a beam dimension of about 0.5 mm. Figure 2. shows a comparison between experimental and simulated unpolarized transmission data for the different gratings. A planar sample, i.e. without grating, but identical epitaxial structure, was used as reference sample. The simulations and measurements are normalized to the maximum value of the reference sample. The spectra show the relevant wavelength region from 2.5 - 5.0

µm. Since the measurements were performed on unpolished and unthinned samples (i.e. through 450 µm thick n-doped substrate), the absolute values differ slightly from the calculated ones obtained by simulating without absorption. This can be explained by optical losses due to diffuse scattering at the unpolished backside of the sample and absorption in the substrate.
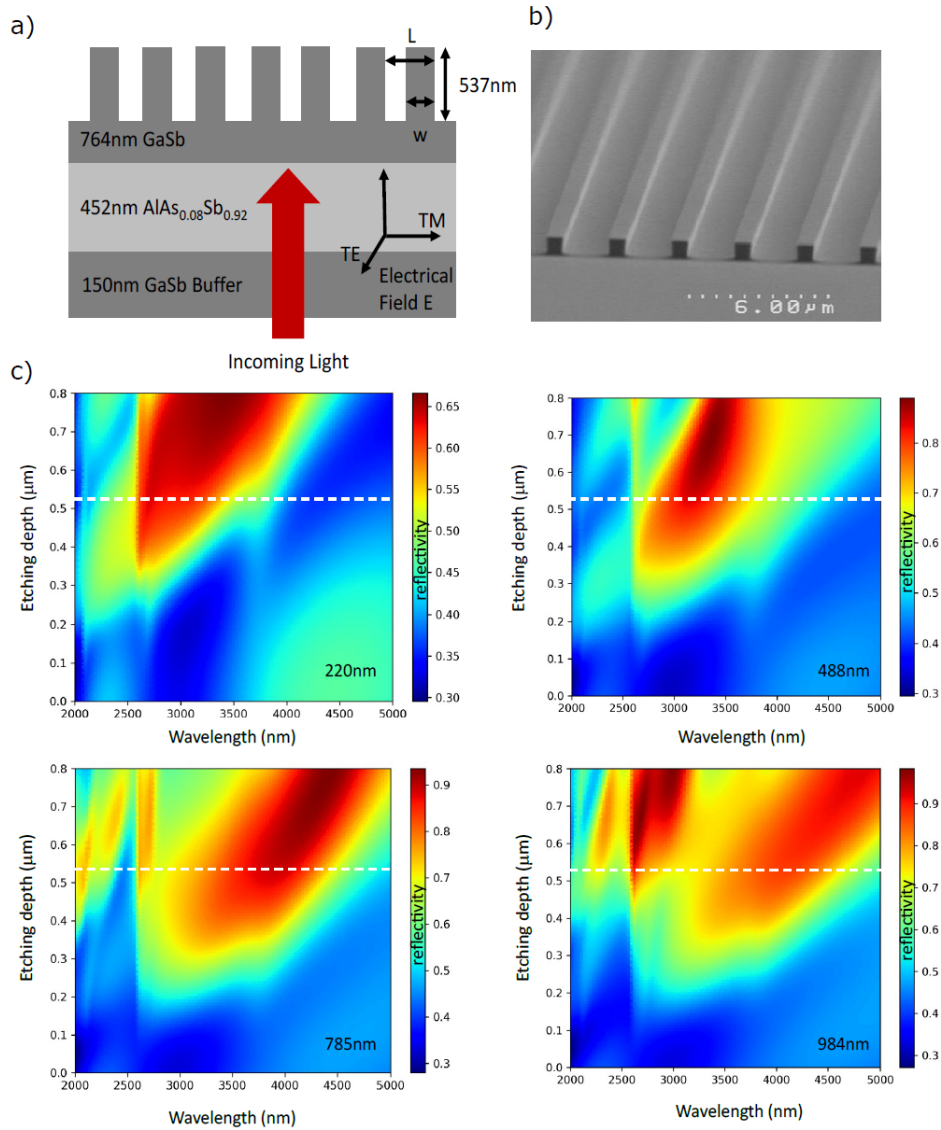

Fig. 1. (a) Schematic heterostructure layout of the MHCG. The grating depth is 537 nm, the grating period is L = 2.6 µm and different ridge widths w = 220, 488, 785, and 984 ± 5 nm were realized in this paper. Measurements and simulations were performed with light incident from the substrate side of the sample. (b) Electron microscope image of the processed grated surface. (c) Simulated reflectivity spectra of the MHCG for unpolarized light for different ridge widths. The colormap demonstrate the flexibility reflection selection regarding ridge width and etching depth.

Since these measurements were performed in atmospheric conditions, the experimental data show H_2O absorption around 2.7 µm and CO_2 absorption around 4.2 µm. In spite of these

discrepancies, the experimental data for all gratings and corresponding reference are overall in good agreement with the simulations and reflect all the main tendencies properly.
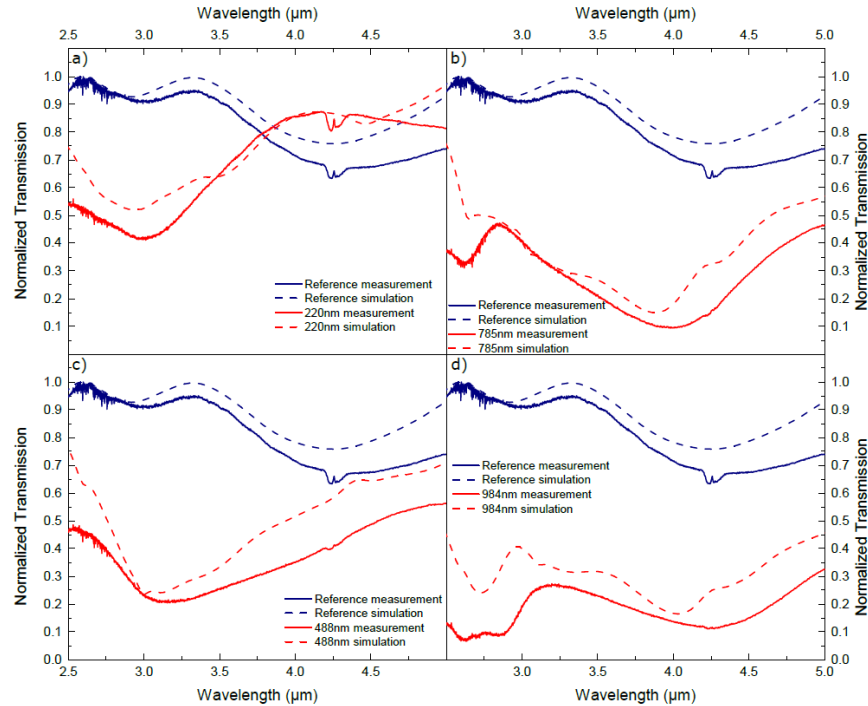

Fig. 2. Normalized transmission (simulated dashed lines, experimental solid lines) for unpolarized light incident from the backside of the sample. Blue colored lines represent the reference sample without etched grating. The red lines represent the experimental and simulated data of the gratings with (a) 220 nm, (b) 488 nm, (c) 785 nm and (d) 984 nm wide ridges. A planar sample, i.e. ,without grating, but identical epitaxial structure, was used as reference sample. The experimental data shows good agreement with the simulation. Deviations result from reflections in other directions due to process imperfections in the real etched grating. The simulation of transmission have been performed with the commercial software Lumerical within the FDTD solver: 3D Electromagnetic Simulator [42].

The transmission, under the assumption of normal light incidence on the backside of the sample can be expressed as follows:

$$T = (1 - R_b) * exp^{-\alpha d} * (1 - R_t) \tag{1}$$

Here R_b is the reflectivity at the substrate side (backside) and exp(-αd) is the absorption of the material with absorption coefficient α, which also includes all possible losses in this case, and thickness d (including 450 µm doped substrate). R_t is the total reflectivity of the surface side, i.e. $R_{t,ref}$ and $R_{t,MHCG}$ for the reference sample and for the MHCG sample, respectively. $R_{t,MHCG}$ is the reflection into all diffraction orders propagating in GaSb. The reference sample is in this case one sample piece from the same wafer, which was cleaved after growth, without MHCG on the surface. For the different grating samples and reference, each R_b and exp(-αd) are assumed to be identical since the samples are from the same wafer and therefore the free carrier absorption in the Te-doped substrate is similar as well as the level of light scattering at unpolished surface are equal. Equation (1) is a simplified approach, which does not take any multiple reflections at the interfaces of the heterostructure into account. This is a valid assumption as interference

effects from the substrate side can be omitted because of the unpolished surface and multiple reflections from the AlGaSb/GaSb interface are accounted by referencing the structure. Thus, the ratio between transmission for reference sample, T_{ref}, and MHCG sample, T_{MHCG}, can be expressed as follows:

$$\frac{T_{MHCG}}{T_{Ref}} = \frac{(1 - R_{t,MHCG})}{(1 - R_{t,Ref})} \quad (2)$$

With Eq. (2) the reflectivity of the MHCG, $R_{t,MHCG}$, can be extracted directly from the transmission measurements:

$$(1 - R_{t,MHCG}) = \frac{T_{MHCG}}{T_{Ref}}(1 - R_{t,Ref}) \quad (3)$$

$R_{t,Ref}$ corresponds to the reflectivity (also including multiple reflections and higher reflection orders) of the unprocessed sample at the interface between GaSb and air in the given heterostructure with light incident from the substrate-side.

From experimental and simulated data, the reflectivity can be determined. Figure 3 shows the calculated reflectivity spectra derived from transmission measurements as described earlier in comparison to the simulated reflection. For $R_{t,Ref}$ the simulated values for the reference (as presented in the simulation in Fig. 1(c)) were used to calculate $R_{t,MHCG}$. The largest experimental
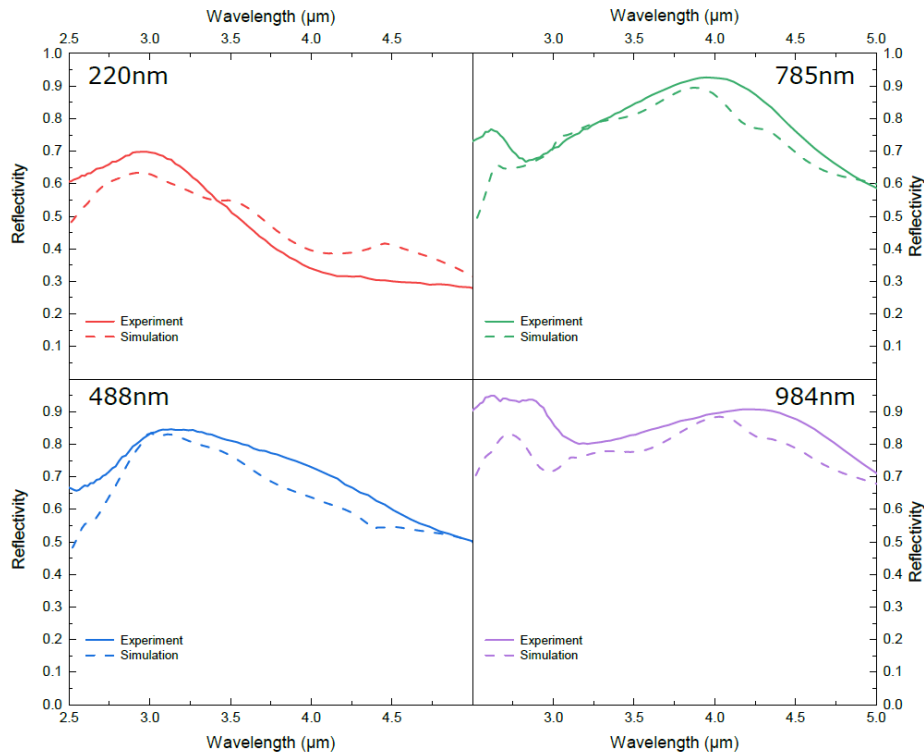

Fig. 3. Comparison between experimental and simulated reflectivity for the gratings with ridge widths between 220 and 984 nm. Reflectivity of up to 0.92 was achieved for the grating with w = 785 nm at 4 μm. The high reflectivity at 2.6 μm for the 984 nm grating corresponds to analysis artefacts. The reflectivity for wavelengths above 3 μm differs only about 0.1 from the simulation which can be attributed to process dependent imperfections of the etched surface gratings. The simulation of reflectivity have been performed with the commercial software Lumerical within the FDTD solver: 3D Electromagnetic Simulator [42].

reflectivity is achieved at the level of 0.92 at 4 μm with the 785 nm grating. Compared to the simulated values, the experimental reflectivities show slightly higher values but are in good agreement with the simulated ones and differ by about 0.1. The calculated reflectivity (Eq. (3)) can reach higher values, which do not represent the actual reflectivity. In shorter wavelengths multiple reflectivity maxima can exist (see Fig. 1(c)) that influence the experimental spectrum contributing to local reflectivity maxima that are not present for all considered grating periods. We determine the reflectivity under the assumption of a perfect grating. This, however, neglects reflections in other directions due to process imperfections of the etched gratings. These assumptions lead to apparently higher calculated reflectivity values exceeding simulated ones, since in the calculations each drop in transmission is considered to correspond to an increase in reflection normal to the growth plane. This does not demonstrate a real increase in reflectivity, compared to the simulated ones.
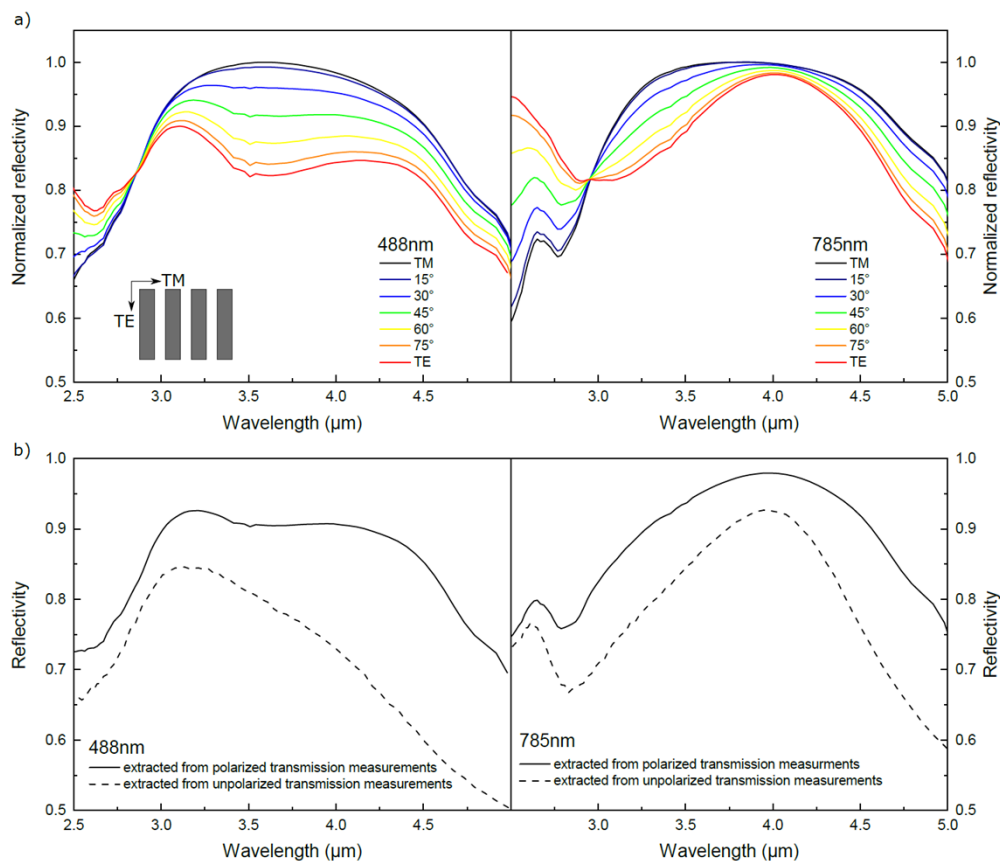

Fig. 4. (a) Normalized polarization dependent reflectivity extracted from transmission measurements of the gratings with 488 and 785 nm wide ridges, respectively. The measurements were performed in steps of 15° from TM to TE polarization. The reflectivity is highest for TM polarized light and decreases towards TE polarized light. The 488 nm grating shows clear polarization selection for reflection of TM polarized light. (b) Comparison between unnormalized reflectivity for unpolarized light extracted from unpolarized and polarized transmission measurements for ridge width of 488 and 785 nm. For extraction from polarized measurements, the reflectivity for TM and TE polarized light was averaged to achieve the reflectivity for unpolarized light.

Finally, polarization dependent transmission measurements were performed from TM to TE polarization in steps of 15 degree in vacuum for two samples with grating widths of w = 488 and 785 nm. The normalized reflectivity (normalized to the maximum of TM polarized reflectivity) extracted from these measurements (analog to unpolarized measurements) are shown in Fig. 4(a). In the case of the 488 nm grating, the local maximum at 3.0 µm does quantitatively change with polarization. When going towards longer wavelengths, polarization dependent reflectivity is observed, being dominated by the TE fraction. The reflectivity for pure TE polarization decreases and reaches a local minimum at 3.6 µm for purely TE-polarized light. For TM-polarized light, the reflectivity is increased achieving a local maximum at approx. 3.6 µm. For the w = 785 nm grating the reflectivity shows local minima at 2.8 µm for TM-polarized light and at 3.0 µm for TE polarized light. At 3.7 µm and 4.0 µm maxima in reflectivity are achieved for TM- and TE-polarization, respectively.

In Fig. 4(b) the unnormalized reflectivity for unpolarized light extracted from unpolarized and polarization dependent transmission measurements is compared. The spectra show consistency regarding qualitative trend of the curve. Quantitatively the reflectivity exctracted from polarization dependent measurements clearly show higher reflectivities since the polarized measurements were performed under 12° angle of incidence, which cause slightly different basic conditions resulting in overrated values of reflectivity in the case of the polarized measurements. These results show that MHCG although imposes polarization selectivity, the high reflectivities for TE and TM polarization can be balanced and provide high reflectivity of unpolarized light.

4. Summary

In conclusion, this paper presents the first experimental demonstration of high reflectivity of unpolarized infrared light from GaSb/AlAsSb MHCG fabricated by electron beam lithography and dry chemical etching. The maximal reflectivity of unpolarized light was at the level of 92%. The structure has also revealed above 75% reflectance broadband tuning range from 3 to 4.3 µm facilitated by modification of the width of MHCG stripes. All experimental results presented in this paper are in excellent agreement with theory, which predicts above 95% reflectivity of unpolarized light for the tested configuration. Such high reflectivity could be achieved experimentally by perfecting the process of grating fabrication. These results pave the way towards the possibility of replacing top epitaxial or dielectric DBR for GaSb based RCLEDs, RCE photodetectors and other optoelectronic devices. The work also proves that MHCGs are a promising candidate for the simplified and cost-effective fabrication of resonator-based optoelectronic devices on GaSb operating in the application relevant range of mid-infrared.

Disclosures. The authors declare no conflicts of interest.

Data availability. Data underlying the results presented in this paper are not publicly available at this time but may be obtained from the authors upon reasonable request.

References

1. E. D. Hinkley, "High resolution infrared spectroscopy with tunable diode laser," Appl. Phys. Lett. **16**(9), 351–354 (1970).
2. P. Werle, "A review of recent advances in semiconductor laser-based gas monitors," Spectrochim. Acta, Part A **54**(2), 197–236 (1998).
3. R. Q. Yang, Z. Tian, J. F. Klem, T. D. Mishima, M. B. Santos, and M. B. Johnson, "Interband cascade photovoltaic devices," Appl. Phys. Lett. **96**(6), 063504 (2010).
4. R. Q. Yang, Z. Tian, Z. Cai, J. F. Klem, M. B. Johnson, and H. C. Liu, "Interband-cascade infrared photodetectors with superlattice absorbers," J. Appl. Phys. (Melville, NY, U. S.) **107**(5), 054514 (2010).

5. R. Q. Yang, "Infrared laser based on intersubband transitions in quantum wells," Superlattices Microstruct. **17**(1), 77–83 (1995).

6. J. R. Meyer, W. W. Bewley, C. L. Canedy, C. S. Kim, M. Kim, C. D. Merritt, and I. Vurgaftman, "The Interband Cascade Laser," Photonics **7**(3), 75 (2020).

7. I. Vurgaftman, R. Weih, M. Kamp, J. R. Meyer, C. L. Canedy, C. S. Kim, M. Kim, W. W. Bewley, C. D. Merritt, J. Abell, and S. Höfling, "Interband cascade lasers," J. Phys. D: Appl. Phys. **48**(12), 123001 (2015).

8. V. Letka, A. Bainbridge, A. P. Craig, F. Al-Saymir, and A. J. Marshall, "Resonant cavity-enhanced photodetector incorporating a type-II superlattice to extend MWIR sensitivity," Opt. Express **27**(17), 23970–23980 (2019).

9. N. Li, L. Tao, H. Yi, C. Soo Kim, M. Kim, C. L. Canedy, C. D. Merritt, W. W. Bewley, I. Vurgaftman, J. R. Meyer, and M. A. Zondlo, "Methane detection using an interband-cascade LED couples to a hollow-core fiber," Opt. Express **29**(5), 7221–7231 (2021).

10. R. Q. Yang, C. Lin, S. J. Murry, S. S. Pei, H. C. Liu, M. Buchanan, and E. Dupont, "Interband cascade light emitting diodes in the 5-8 μm spectrum region," Appl. Phys. Lett. **70**(15), 2013–2015 (1997).

11. J. Abell, C. S. Kim, W. W. Bewley, C. D. Merritt, C. L. Canedy, I. Vurgaftman, J. R. Meyer, and M. Kim, "Mid-infrared interband cascade light emitting devices with milliwatt output powers at room temperature," Appl. Phys. Lett. **104**(26), 261103 (2014).

12. N. Schäfer, J. Scheuermann, R. Weih, J. Koeth, and S. Hoefling, "High efficiency mid-infrared interband cascade LEDs grown on low absorbing substrates emitting > 5 mW of output power," Opt. Eng. **58**(11), 1 (2019).

13. H. Yokoyama, K. Nishi, T. Anan, H. Yamada, S. D. Brorson, and E. P. Ippen, "Enhanced spontaneous emission from GaAs quantum wells ind monolithic microcavities," Appl. Phys. Lett. **57**(26), 2814–2816 (1990).

14. E. F. Schubert, A. M. Vredenberg, N. E. J. Hunt, Y. H. Wong, P. C. Becker, J. M. Poate, D. C. Jacobson, L. C. Feldman, and G. J. Zydzik, "Giant Enhanement of luminescence intensity in Er-doped Si/SiO2 resonant cavities," Appl. Phys. Lett. **61**(12), 1381–1383 (1992).

15. N. E. J. Hunt, E. F. Schubert, R. F. Kopf, D. L. Sivco, A. Y. Cho, and G. J. Zydzik, "Increased fibre communications bandwith from a resonator cavity light emitting diode emitting at λ=940 nm," Appl. Phys. Lett. **63**(19), 2600–2602 (1993).

16. A. Dodabalapur, L. J. Rothberg, and T. M. Miller, "Color variation with electroluminescent organic semiconductors in multimode resonant cavities," Appl. Phys. Lett. **65**(18), 2308–2310 (1994).

17. K. Streubel, U. Helin, V. Oskarsson, E. Bäcklin, and A. Johansson, "High Brightness Visible (660 nm) Resonant-Cavity Light-Emitting Diode," IEEE Photonics Technol. Lett. **10**(12), 1685–1687 (1998).

18. D. A. Diaz-Thomas, O. Stepanenko, M. Bahriz, S. Calvez, T. Batte, C. Paranthoen, G. Patriarche, E. Tournié, A. N. Baranov, G. Almuneau, C. Levallois, and L. Cerutti, "3.3 μm interband-cascade resonant-cavity light-emitting diode with narrow spectral emission linewidth," Semicond. Sci. Technol. **35**(12), 125029 (2020).

19. M. S. Ünlü, K. Kishino, H. J. Liaw, and H. Morkoc, "A theoretical study of resonant cavity-enhanced photodetectors, with Ge and Si active regions," J. Appl. Phys. (Melville, NY, U. S.) **71**(8), 4049–4058 (1992).

20. A. P. Craig, F. Al-Saymari, M. Jain, A. Bainbridge, G. R. Savich, T. Golding, A. Krier, G. W. Wicks, and A. R. Marchall, "Resonant cavity enhanced photodiodes on GaSb for the mid-wave infrared," Appl. Phys. Lett. **114**(15), 151107 (2019).

21. S. Wang, "Principles of Distributed Feedback and Distributed Bragg-Reflector Lasers," IEEE J. Quantum Electron. **10**(4), 413–427 (1974).

22. Y. H. Lee, J. L. Jewell, A. Scherer, S. L. McCall, S. J. Walker, J. P. Harbison, and L. T. Florez, "Room-temperature continouse-wave vertical- cavity single-quantum-well microlaser diodes," Electron. Lett. **25**(20), 1377–1378 (1989).

23. A. Ducanchez, L. Cerutti, P. Grech, F. Genty, and E. Tournie, "Mid-infrared GaSb-based EP-VCSEL emitting at 2.63 μm," Electron. Lett. **45**(5), 265–267 (2009).

24. W. Bewley, C. Canedy, C. Kim, C. Merritt, M. V. Warren, I. Vurgaftman, J. R. Meyer, and M. Kim, "Roomt-temperature mid-infrared interband cascade vertical-cavity surface-emitting lasers," Appl. Phys. Lett. **109**(15), 151108 (2016).

25. F. Koyama, S. Kinoshita, and K. Iga, "Room-temperature continuous wave lasing characteristics of a GaAs vertical cavity surface-emitting laser," Appl. Phys. Lett. **55**(3), 221–222 (1989).

26. A. Andrejew, S. Sprengel, and M.-C. Amann, "GaSb-based vertical cavity surface-emitting lasers with an emission wavelength at 3 μm," Opt. Lett. **41**(12), 2799–2802 (2016).

27. C. S. Kim, W. Bewley, C. Merritt, C. L. Canedy, M. V. Warren, I. Vurgaftman, J. R. Meyer, and M. Kim, "Improved mid-infrared interband cascade light-emitting devices," Opt. Eng. **57**(01), 1 (2017).

28. G. Veerabathran, S. Sprengel, A. Andrejew, and M.-C. Amann, "Room-temperature vertical-cavity surface-emitting lasers at 4 μm with GaSb-based type-II quantum wells," Appl. Phys. Lett. **110**(7), 071104 (2017).

29. C. F. R. Mateus, M. C. Y. Huang, L. Chen, and C. J. Chang-Hasnain, "Broad-Band Mirror (1.12-1.62 μm) using a subwavelength grating," IEEE Photonics Technol. Lett. **16**(7), 1676–1678 (2004).

30. Y. Zhou, M. C. Y. Huang, C. Chase, V. Karagodsky, M. Moewe, B. Pesala, F. G. Sedgwick, and C. J. Chang-Hasnain, "High-Index-Contrast Grating (HCG) and its applications in optoelectronic devices," IEEE J. Sel. Top. Quantum Electron. **15**(5), 1485–1499 (2009).

31. M. C. Y. Huang, Y. Zhou, and C. J. Chang-Hasnai, "A surface-emitting laser incorporating a high-index-contrast subwavelength grating," Nat. Photonics **1**(2), 119–122 (2007).

32. M. C. Y. Huang, Y. Zhou, and C. J. Chang-Hasnai, "A nanoelectronical tunable laser," Nat. Photonics **2**(3), 180–184 (2008).

33. M. Gębski, M. Dems, A. Szerling, M. Motyka, L. Marona, R. Kruszka, D. Urbańczyk, M. alczakowski, N. Pałka, A. Wójcik-Jedlińska, Q. J. Wang, D. H. Zhang, M. Bugajski, M. Wasiak, and T. Czyszanowski, "Monolithic high-index contrast grating: a material independent high reflectance VCSEL mirror," Opt. Express **23**(9), 11674–11686 (2015).

34. T. Czyszanowski, M. Gębski, E. Pruszyńska-Karbownik, M. Wasiak, and J. A. Lott, "Monolithic high-contrast grating planar microcavities," Nanophotonics **9**(4), 913–925 (2020).

35. M. Dems, "Modelling of high-contrast grating mirrors. The impact of imperfections on their performance in VCSELs," Opto-Electron. Rev. **19**(3), 340 (2011).

36. J. Petykiewicz, *Wave Optics* (Springer, 2010).

37. M. Marciniak, M. Gęebski, M. Dems, E. Haglund, A. Larsson, M. Riaziat, J. A. Lott, and T. Czyszanowski, "Optimal parameters of monolithic high contrast grating mirrors," Opt. Lett. **41**(15), 3495–3498 (2016).

38. M. Marciniak, A. Broda, M. Gęebski, M. Dems, J. Muszalski, A. Czerwiński, A. Ratajczak, Ł Marona, W. Nakwaski, J. A. Lott, and T. Czyszanowski, "Tuning of reflection spectrum of a monolithic highcontrast grating by variation of its spatial dimensions," Opt. Express **28**(14), 20967–20977 (2020).

39. M. Motyka and J. Misiewicz, "Fast Differential Reflectance Spectroscopy of Semiconductor Structures for Infrared Applications by Using Fourier Transform Spectrometer," Appl. Phys. Express **3**(11), 112401 (2010).

40. M. Motyka, G. Sek, F. Janiak, J. Misiewicz, K. Klos, and J. Piotrowski, "Fourier-transformed photoreflectance and fast differential reflectance of HgCdTe layers. The issues of spectral resolution and Fabry-Perot oscillations," Meas. Sci. Technol. **22**(12), 125601 (2011).

41. M. Rygała, K. Ryczko, T. Smołka, D. Kujawa, P. Martyniuk, T. J. Ronningen, S. Krishna, and M. Motyka, "Investigating the physics of higher-order optical transitions in InAs/GaSb superlattices," Phys. Rev. B **104**(8), 085410 (2021).

42. Lumerical Inc., https://www.lumerical.com/products/.